White Rose Research Online

eprints@whiterose.ac.uk
https://eprints.whiterose.ac.uk
Universities of Leeds, Sheffield and York

Deposited via The University of Sheffield.

White Rose Research Online URL for this paper:
https://eprints.whiterose.ac.uk/id/eprint/247199/

Version: Accepted Version

Article:
Kamal, T., Ranot, H., Mandal, S. et al. (2026) CALPHAD coupled experimental investigation of structure–property evolution in solute lean Cu–Ni–Sn alloys. Journal of Alloys and Compounds, 1082. 191496. ISSN: 0925-8388

https://doi.org/10.1016/j.jallcom.2026.191496

© 2026 The Authors. Except as otherwise noted, this author-accepted version of a journal article published in Journal of Alloys and Compounds is made available via the University of Sheffield Research Publications and Copyright Policy under the terms of the Creative Commons Attribution 4.0 International License (CC-BY 4.0), which permits unrestricted use, distribution and reproduction in any medium, provided the original work is properly cited. To view a copy of this licence, visit http://creativecommons.org/licenses/by/4.0/

Reuse
This article is distributed under the terms of the Creative Commons Attribution (CC BY) licence. This licence allows you to distribute, remix, tweak, and build upon the work, even commercially, as long as you credit the authors for the original work. More information and the full terms of the licence here: https://creativecommons.org/licenses/

Takedown
If you consider content in White Rose Research Online to be in breach of UK law, please notify us by emailing eprints@whiterose.ac.uk including the URL of the record and the reason for the withdrawal request.

UNIVERSITY OF LEEDS
University of Sheffield
UNIVERSITY of York

CALPHAD coupled experimental investigation of structure–property evolution in solute lean Cu–Ni–Sn alloys

Tafzeelul Kamal[a,c], Harish Ranot[b], Swapnadeep Mandal[c], Mirtunjay Kumar[d], Anish Upadhyaya[c,*]

[a]*Department of Metallurgical and Materials Engineering, Indian Institute of Technology Kharagpur, West Bengal, India*
[b]*School of Minerals, Metallurgical and Materials Engineering, Indian Institute of Technology Bhubaneswar, India*
[c]*Department of Materials Science and Engineering, Indian Institute of Technology Kanpur, Uttar Pradesh, India*
[d]*School of Chemical, Materials and Biological Engineering, The University of Sheffield, Sheffield, South Yorkshire, United Kingdom*

Abstract

The transition towards low-Sn content alloy design represents a promising avenue for developing high-performance Cu–Ni–Sn alloys, enabling tailored microstructural evolution while minimizing the propensity for undesirable secondary phase formation. Accordingly, the present work presents a CALPHAD-coupled experimental investigation to elucidate the influence of Sn addition on microstructural characteristics and resulting properties of solute-lean Cu–Ni–Sn alloys. The alloys were synthesised using powder metallurgy route, wherein the Ni content was fixed at 4 wt%, while the Sn

*Corresponding author.
Email address: anishu@iitk.ac.in (Anish Upadhyaya)

concentration was systematically varied from 0 to 4 wt%. The experimental findings closely corroborated the thermodynamic predictions, revealing that Sn additions up to 3 wt% preserve an FCC-dominated microstructure containing only a limited amount of solute-rich precipitates. Progressive enhancement in densification was observed with increasing Sn content from 0 to 3 wt%, where Cu–4Ni–3Sn alloy achieved the highest relative sintered density (∼91%), corresponding to an improvement of ∼11% over Cu–4Ni alloy. In contrast, further increasing the Sn content to 4 wt% resulted in reduced densification and a marked deterioration in electrical conductivity. Moreover, the compressive yield strength of Cu–4Ni–3Sn alloy exhibited more than two-fold increase relative to the Cu–4Ni alloy, with only marginal strengthening thereafter, indicating the onset of strength saturation with further Sn addition. Collectively, the findings obtained in this study demonstrate that judicious incorporation of 3 wt% Sn represents an effective solute-lean alloy design strategy for achieving a favourable combination of densification, strength and electrical conductivity in sintered Cu–Ni–Sn alloys.

Keywords:

Powder metallurgy, Sintering, CALPHAD, Microstructure, Densification, Strength

---

1. Introduction

Cu–Ni–Sn alloys have garnered significant interest and emerged as notable alternatives to Cu–Be alloys in electronics, aerospace and marine sectors, owing to their remarkable combination of strength, electrical conductivity, wear resistance and corrosion resistance [1, 2]. However, Cu–Ni–Sn alloys with high Ni and Sn contents fabricated through conventional processing route of casting typically exhibit electrical conductivities below 12% IACS (International Annealed Copper Standard), which are considerably lower than those of Cu–Be alloys [3, 4]. Moreover, despite the exceptional strength attainable in Cu–Ni–Sn alloys, macro-segregation of Sn remains a persistent challenge in conventionally processed compositions, particularly at higher Sn contents, owing to the limited solubility of Sn in Cu, the wide solidification temperature interval and the substantial differences in melting point of the constituent elements [5]. During the casting process, solidification of Cu–Ni–Sn alloys is accompanied by dendritic microstructure formation and Sn segregation, resulting in compositional heterogeneity that promotes the formation of solute-rich regions and brittle intermetallic phases, which collectively deteriorate mechanical and electrical properties, reduce workability, and hinder subsequent thermomechanical processing, thereby making the fabrication of thin sheet products particularly challenging [6, 7]. These processing limitations inherent to high Sn content Cu–Ni–Sn alloys have motivated the development of solute-lean alloy design strategies for regulating microstructural evolution while retaining a desirable combination of strength

and electrical conductivity. Nevertheless, the selection of an appropriate processing technique is equally vital in order to fully exploit the potential of the designed alloy compositions. In this regard, powder metallurgy (PM) offers an attractive alternative processing route that employs temperatures substantially lower than those required during conventional casting. Moreover, the relatively low processing temperatures employed in PM route foster diffusion-mediated microstructural evolution without requiring complete melting and subsequent solidification, thereby enabling the development of compositionally engineered Cu–Ni–Sn alloys with tailored phase constitution and properties. Despite these advantages, the composition-dependent interplay between thermodynamic phase stability, microstructural evolution and resultant properties in solute-lean Cu–Ni–Sn alloys processed through PM remains largely unexplored.

Most of the reported studies on Cu–Ni–Sn alloys have focused on alloying driven structure–property tailoring and thermomechanical processing of cast alloys [8, 9, 10, 11], with particular emphasis on high Sn compositions, aging-induced precipitation and spinodal decomposition [2, 4, 12, 13, 14]. In contrast, comparatively little attention has been devoted to the development of solute lean Cu–Ni–Sn alloys based on thermodynamic phase stability predictions in conjunction with PM processing. Although previous CALPHAD investigations of the Cu–Ni–Sn alloy system have established reliable descriptions of phase stability across a broad compositional range [15, 16], their scope has largely been limited to thermodynamic predictions

without demonstrating how these predicted results translate into the experimentally observed phase constitution under practical processing circumstances. The present work addresses this gap by integrating equilibrium thermodynamic predictions with PM processing to establish composition–processing–microstructure–property correlation in solute lean Cu–Ni–Sn alloys in which relatively small compositional changes can significantly affect the phase stability and resulting properties. Instead of employing CALPHAD solely as a predictive thermodynamic tool, the present work elucidates the experimental manifestation of equilibrium thermodynamic predictions in the phase evolution occurring under practical PM processing conditions. Particular emphasis is placed on delineating the compositional regime that promotes the stability of the Cu-rich face-centred cubic (FCC) solid solution while limiting the formation of solute-rich secondary phases. By integrating thermodynamic predictions with experimental findings, this study presents a holistic framework for elucidating the role of solute lean alloying in governing the structure–property evolution, thereby providing a rational pathway for the development of high-performance Cu–Ni–Sn alloys.

2. Methodology

2.1. Computational thermodynamic analysis

The CALPHAD approach was employed for predicting phase equilibria and thermodynamic stability across the range of studied compositions. The

computational thermodynamic study was carried out by utilising Thermo-Calc software [17] using the TCCU6 thermodynamic database. In this study, the concentration of Ni was fixed at 4 wt% to minimizing excessive degradation in electrical conductivity, as higher Ni additions are known to significantly increase electron scattering in Cu alloys [18]. In contrast, the Sn content was varied from 0 to 4 wt% to systematically probe the transition from Sn-free to the upper limit of the solute-lean regime reported in the literature [7, 19], where the interplay among phase stability, precipitation tendency and resultant properties could be critically assessed. Guided by the thermodynamic predictions, the selected alloys were subsequently synthesized via PM processing and subjected to comprehensive characterization to establish the composition–microstructure–property relationship.

2.2. Alloy processing

In the present work, elemental powders of copper (Cu), nickel (Ni) and tin (Sn) were utilized as starting materials. SEM micrographs depicting the morphology of the powders are shown in Fig. 1. Further details of the powders employed for the synthesis of Cu–Ni–Sn alloys are listed in Table 1.

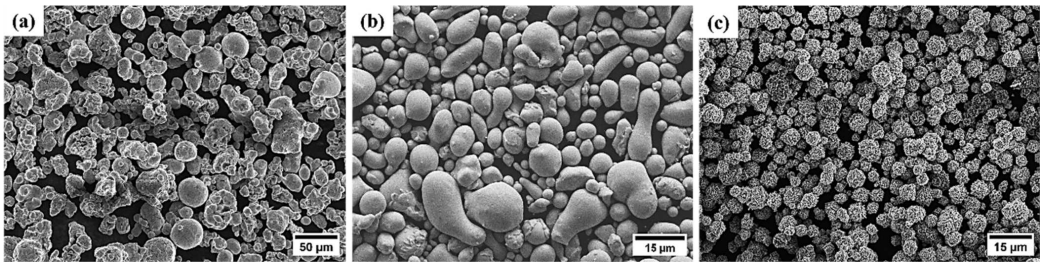


Figure 1: SEM micrographs of (a) Cu; (b) Sn and (c) Ni powders.

Table 1: Details of raw materials.

Element	Supplier	Purity (%)	Average particle size (μm)	Theoretical density (g/cm^3)	Shape
Cu	Metal Powder Company Ltd., Tamilnadu, India	99	20	8.96	Spheroidal
Ni	Sigma Aldrich, U.S.A	99.99	5	8.90	Spheroidal (spiky)
Sn	Metal Powder Company Ltd., Tamilnadu, India	99	10	7.31	Non-spherical

Elemental powder blends were formulated according to the following compositions (in weight %): Cu–4Ni, Cu–4Ni–1Sn, Cu–4Ni–2Sn, Cu–4Ni–3Sn, and Cu–4Ni–4Sn. The required quantities of each elemental powder were weighed using an analytical balance with $\pm$0.0001 g accuracy. Subsequently the powder mixture consisting of Cu, Ni and Sn corresponding to the designed compositions were thoroughly blended for 3 h in a turbula mixer to ensure uniform mixing. The pre-mixed powder blends were uniaxially compacted in a cylindrical die using a hydraulic press. A compaction pressure of 400 MPa was applied to form cylindrical green compacts with dimensions of 12 mm diameter $\times$ 6 mm height. The green compacts were sintered in a conventional tubular furnace. Before the initiation of sintering, the furnace tube was purged with argon gas to displace residual air and establish an inert atmosphere. Hydrogen gas was then introduced in the tube, and the green compacts were subsequently sintered under a controlled hydrogen atmosphere. The samples were heated from room temperature to 900 °C

at a constant heating rate of 5 °C min^{-1}, held at 900 °C for 1 h, and subsequently furnace cooled to room temperature under the same atmosphere. A schematic representation of the complete sintering cycle employed in this study is presented in Fig. 2.

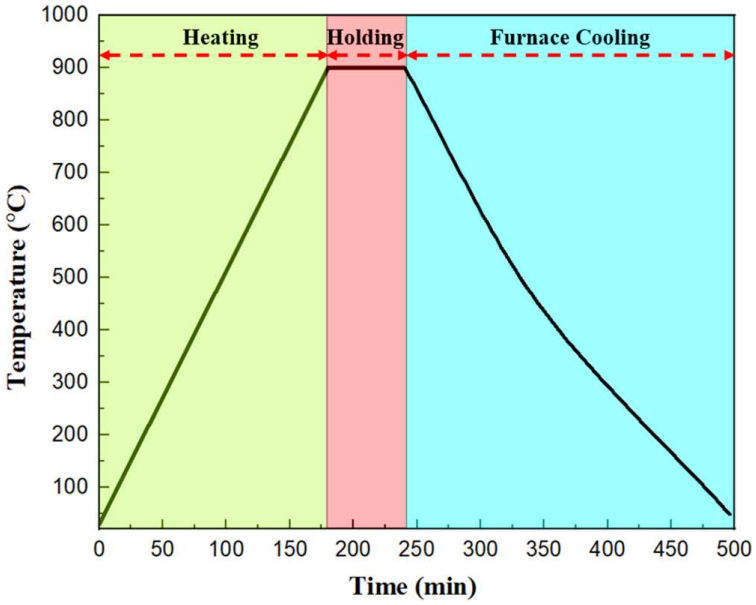


Figure 2: Sintering cycle for synthesis of Cu–Ni–Sn alloys.

2.3. Alloy characterization

The density of sintered compacts was determined using Archimedes principle. Relative sintered density (RD, %Theoretical) and theoretical density (ρ_t) were calculated using Eqs. (1) and (2), respectively [20].

$$RD = \frac{\rho_s}{\rho_t} \times 100 \tag{1}$$

$$\rho_t = \frac{\sum_{i=1}^{n} w_i\%}{\sum_{i=1}^{n} \left[\frac{w_i\%}{\rho}\right]_i} \tag{2}$$

where ρ_s and ρ_t denote the sintered and theoretical densities of the compacts, while the weight percentage and density of individual components are represented by w_i and ρ_i, respectively. Phase identification was conducted using X-ray diffraction (Bruker D8 Focus) with Cu-Kα radiation (wavelength = 1.54 Å). Diffraction patterns were collected over a 2θ range of 20° to 100° at a scanning rate of 2° per minute. Microstructural examination was carried out using scanning electron microscope (SEM) (Zeiss Evo 50) on as-polished samples. Energy-dispersive X-ray spectroscopy (EDS) was utilized to investigate the elemental distribution in the sintered samples. Electron backscatter diffraction (EBSD) experiments were conducted to study the evolution of the grain size of the sintered alloy samples using field emission SEM (Supplier: JEOL, Model: JSM-7100F). EBSD scans were performed at an operating voltage of 20 kV with a step size 0.2 μm. Electrical conductivity was determined utilizing a conductivity meter which was calibrated using annealed Cu with an electrical conductivity of 100% IACS. Hardness measurements were performed by employing a Vickers hardness tester under an applied load of 300 g with a dwell time of 10 s. For each alloy composition, 5 indentations were made at randomly selected locations on the polished surface. To avoid overlap of the plastic deformation fields, adjacent indentations were separated by a centre-to-centre distance of at least three times the average

indentation diagonal length. For compression testing, specimens with a diameter of 4 mm and a height of 6 mm were machined from each sintered compact. The dimensions of the specimen were chosen to attain a height-to-diameter ratio (H/D) of 1.5, in compliance with the ASTM E9 standard. Compression tests were carried out at a constant strain rate of 0.001 s^{-1} using a universal testing machine (INSTRON 5500 R, UK). For each composition, three samples were tested. The compressive yield strength was determined using the 0.2% offset method. A line was drawn parallel to the initial linear elastic segment of the compressive stress–strain curve, offset by a strain of 0.002, and the stress at its intersection with the experimental stress–strain curve was designated as the compressive yield strength. This comprehensive characterization approach enabled a detailed evaluation of microstructural evolution and resulting properties of sintered Cu–Ni–Sn alloys as a function of composition.

3. Results

3.1. Thermodynamic analysis

In this section, the effect of compositional variation on thermodynamic stability and phase equilibria in the Cu–Ni–Sn system is elucidated through a CALPHAD based approach.

The thermodynamic phase-stability predictions obtained using Thermo-Calc, together with the corresponding phase nomenclature and chemical compositions of the phases identified in the calculated phase diagrams are presented in Figs. 3 and 4 and Table 2, respectively. The calculated isothermal section at 900 °C [Fig. 3(a)] shows that the investigated compositions are located within the single-phase stability region at the sintering temperature under equilibrium conditions, indicating that the Cu rich FCC phase is the thermodynamically stable phase expected to exist at this temperature. This phase stability indicates that 900 °C is an appropriate sintering temperature, as it preserves a stable FCC matrix and suppresses secondary phase formation. This prediction is further strengthened by the isopleth section at a constant 4 wt% Ni [Fig. 3(b)], which shows that the studied compositions remain within the FCC phase field during the high-temperature sintering regime and approach the solvus boundary only during subsequent cooling. The computed isopleth section further illustrates that increasing the Sn content from 0 to 4 wt% progressively decreases the solidus temperature from S_0 to S_4 as depicted in Fig. 3(b). The reduction in solidus temperature implies that, at the fixed sintering temperature employed in the present study, the alloys are processed progressively closer to their solidus. Such a thermodynamic shift is anticipated to improve atomic mobility and facilitate diffusion-controlled mass transport during sintering, ultimately promoting densification. Simultaneously, the isopleth section indicates that increasing the Sn content progressively raises the temperature at which the secondary

intermetallic phases first attain thermodynamic stability upon cooling from the sintering temperature. This is accompanied by a corresponding contraction of the single-phase FCC field, indicating a progressive reduction in the temperature range over which the Cu-rich FCC solid solution remains the sole equilibrium phase. Consequently, the thermodynamic stability range of the intermetallic phases expands during cooling from the sintering temperature, indicating an increased tendency for compositional partitioning in the Cu–Ni–Sn system. However, the two aforementioned thermodynamic repercussions evolve concurrently in opposite directions. While increasing Sn content progressively lowers the solidus temperature, excessive Sn addition simultaneously promotes greater equilibrium stability of intermetallic compounds and reduces the thermodynamic stability range of the FCC matrix. The phase fraction diagram depicted in Fig. 4 clearly supports this trend, demonstrating that up to 3 wt% Sn addition, Cu rich FCC phase remains the dominant equilibrium phase, where only a limited phase fraction of secondary intermetallic phase is predicted to exist. As soon as the Sn content reached 4 wt%, the equilibrium fraction of intermetallic phase significantly increases to > 0.1 along with a noticeable reduction in the FCC phase fraction [Fig. 4(e)]. The increasing thermodynamic stability of secondary intermetallic phase with increasing Sn content is expected to promote greater partitioning of solute elements from the Cu-rich matrix (particularly in Cu–Ni–Sn alloys containing $\geq$3 wt% Sn), resulting in enhanced compositional heterogeneity and a higher volume fraction of solute enriched intermetallic constituents upon cooling.

Such microstructural heterogeneity may also influence the mass-transport mechanisms and densification kinetics operative during sintering, thereby impeding pore elimination and limiting the extent of densification. Therefore, although increasing the Sn content provides more favourable thermodynamic conditions for diffusional mass transport, the accompanying increase in elemental partitioning resulting from secondary intermetallic phase formation is likely to offset these beneficial effects. Overall, the thermodynamic predictions indicate that Sn additions up to 3 wt% favour an FCC-dominated phase evolution with only a limited tendency for secondary-phase formation, while avoiding a compositional regime where excessive intermetallic phase formation significantly undermines the stability of the FCC matrix. This phase-stability condition is expected to promote diffusion-assisted neck growth and pore shrinkage while retaining FCC matrix continuity, thereby contributing to a more uniform microstructure and enhanced densification. Here, it is important to mention that the CALPHAD calculations presented here are based on the assumption of thermodynamic equilibrium, and were intended to assess the influence of composition on thermodynamic stability and phase transformation behaviour, rather than to predict the exact phase fractions in sintered Cu–Ni–Sn alloys. Moreover, the kinetic effects associated with finite diffusion rates and other non-equilibrium phenomena during sintering are not explicitly considered in the present calculations. Therefore, the computed phase equilibria describe the thermodynamically stable end state of the alloy under investigation. While kinetic approaches, including

Scheil–Gulliver and DICTRA simulations, could provide further insight into these non-equilibrium phenomena, they are beyond the scope of the present investigation. Future studies incorporating kinetic simulations may provide additional insight into the evolution of non-equilibrium phase transformations during PM processing. The subsequent experimental investigations are presented to elucidate how these equilibrium thermodynamic predictions are manifested during practical PM processing conditions and influence the resulting microstructural evolution and properties.

Table 2: Nomenclature of the phases present in the phase diagrams.

Phase label	Actual phase name	Cu (wt%)	Ni (wt%)	Sn (wt%)	Cu (at%)	Ni (at%)	Sn (at%)
CUSN_GAMMA	High-temperature γ-$(Cu,Ni)_3Sn$	30.9	30.4	38.6	36.5	39.0	24.5
FCC_L12	Cu-rich FCC solid solution	93.0	3.3	3.7	94.4	3.6	2.0
FCC_L12#2	Ni-rich FCC solid solution	0.3	99.7	0	0.28	99.72	0
AG3SN_L60	Low-temperature $(Ni,Cu)_3Sn$	12.4	47.7	39.9	14.5	60.5	25.0
CU3SN	Low-temperature $(Cu,Ni)_3Sn$	40.9	20.1	39.0	49.0	26.0	25.0

3.2. Densification behaviour

Effect of varying composition on the relative sintered density (% theoretical) of PM processed Cu–Ni–Sn alloys is illustrated in Fig. 5(a). It is evident that increase in Sn content leads to increase in the sintered density of the alloy. Among all the sintered samples, the Cu–4Ni–3Sn alloy exhibits the highest sintered density of ∼91%, which is almost 11% more than that

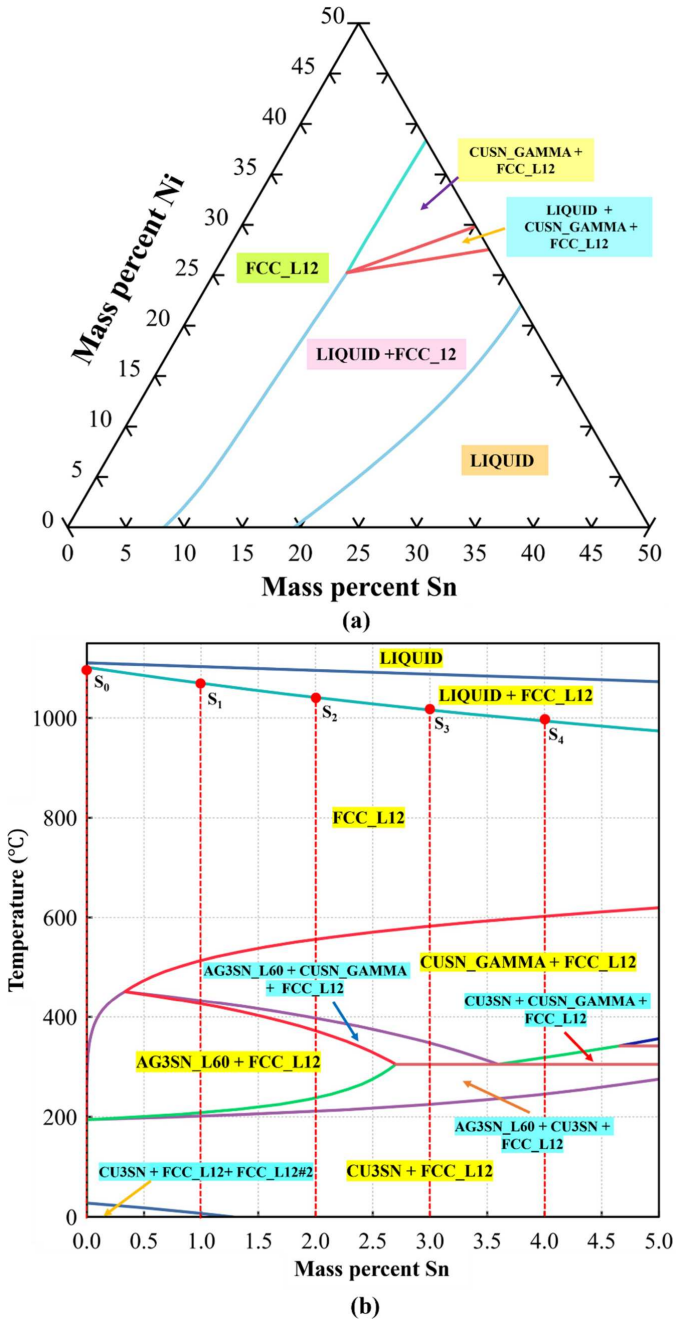


Figure 3: (a) Calculated isothermal section at 900 °C and (b) isopleth section of the Cu–Ni–Sn system at 4 wt% Ni.

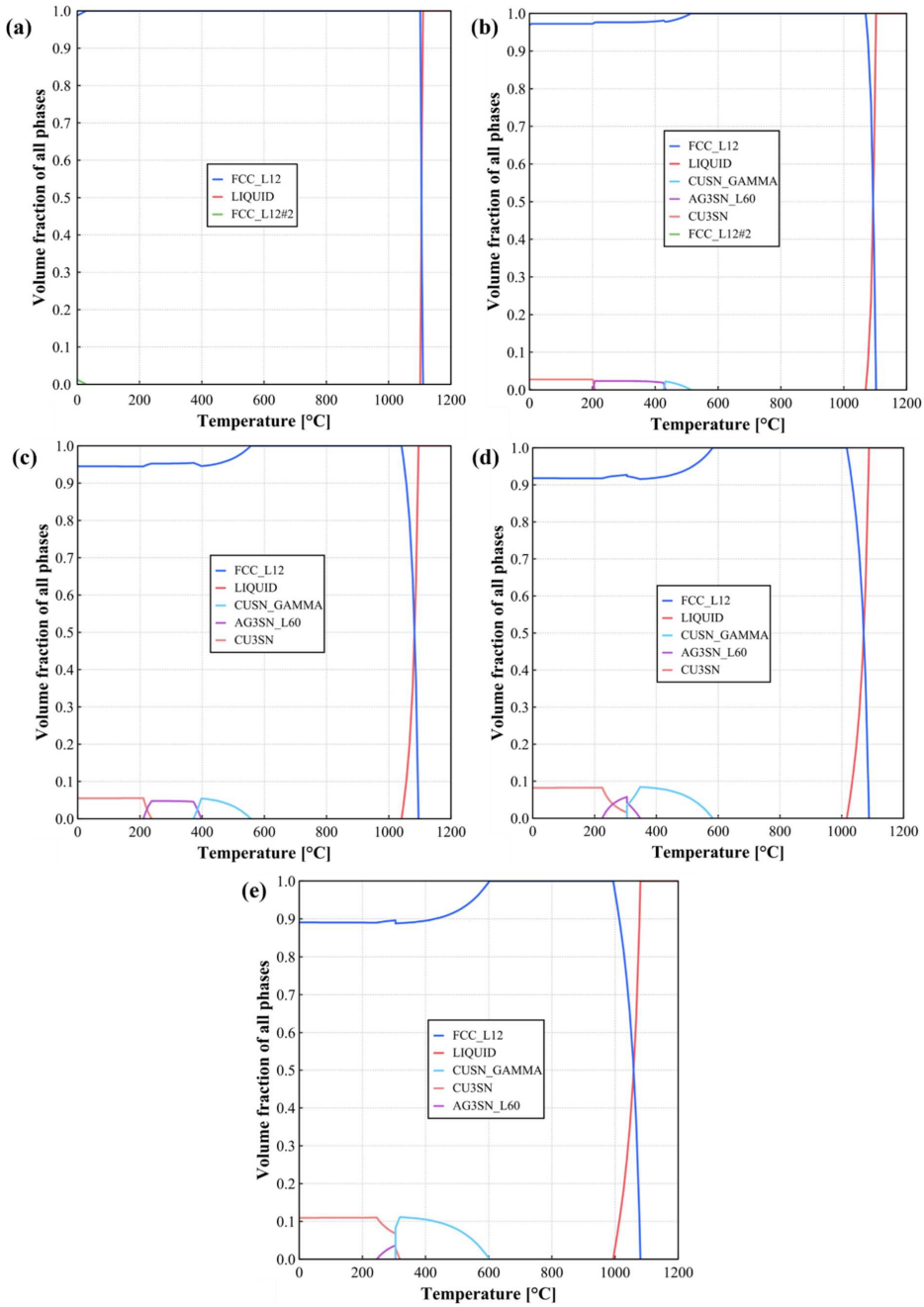


Figure 4: Variation of volume fraction of different phases with temperature in (a) Cu–4Ni; (b) Cu–4Ni–1Sn; (c) Cu–4Ni–2Sn; (d) Cu–4Ni–3Sn; and (e) Cu–4Ni–4Sn alloys.

of Cu–4Ni alloy. Such variations in sintered density can be rationalized by evaluating the extent of densification achieved after sintering. The sintered density of an alloy is influenced by both the shrinkage occurring during sintering and its green density. Consequently, the relative sintered density lacks the ability to accurately represent the volumetric reduction that occurs during the sintering process.

To facilitate the comparison of sintering shrinkage across various compositions, an additional parameter known as densification parameter (DP) has been calculated. The following formula was employed to determine DP [21]:

$$\text{Densification Parameter} = \frac{\text{Sintered Density} - \text{Green Density}}{\text{Theoretical Density} - \text{Green Density}} \tag{3}$$

The definition of DP takes into account the impact of green density. As a result, it serves as a more reliable parameter for quantifying sintering-induced volumetric changes and in turn determining the extent of densification and the underlying reasons for variations in the sintered relative density. A positive value of DP implies shrinkage whereas a negative value signifies expansion. The densification parameter graph of the sintered samples is shown in Fig. 5(b). Bars above the red reference line represent alloy compositions that promote sintering, whereas bars below the line indicate alloy compositions that inhibit sintering. It is evident that the incorporation of Sn up to a certain extent enhances the densification behaviour of Cu–Ni–Sn alloys by

promoting maximum shrinkage during sintering. In particular, the addition of 3 wt% Sn yields the most pronounced densification enhancement, as evident from the highest DP value. As a result, Cu–4Ni–3Sn alloy attains the highest sintered density among the investigated compositions. Collectively, the obtained results demonstrate that Sn addition plays a crucial role in governing the densification behaviour of PM processed Cu–Ni–Sn alloys.

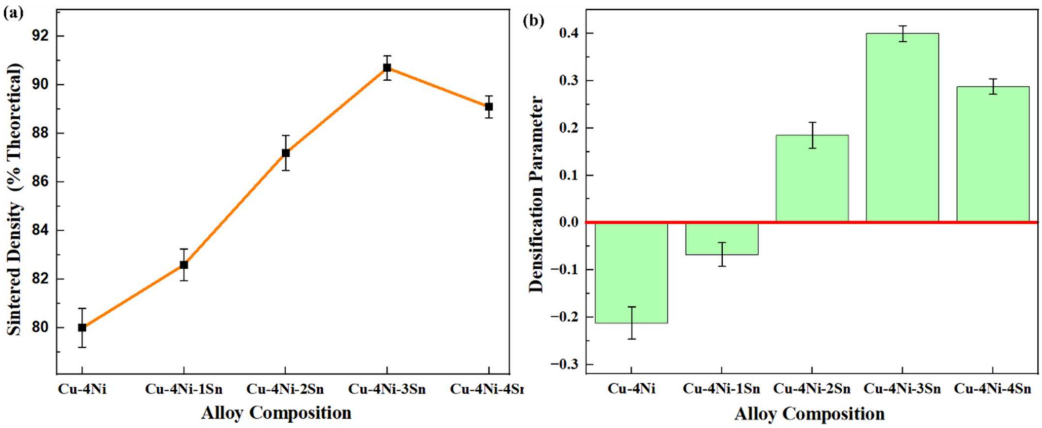


Figure 5: Variation of (a) sintered density; and (b) densification parameter with alloy composition.

3.3. Microstructure

Fig. 6 shows the X-ray diffraction (XRD) patterns of the PM processed samples, indicating that the phase constitution of sintered Cu–Ni–Sn alloys is dominated by a face-centred cubic (FCC) Cu (Ni, Sn) solid solution. Additionally, the XRD pattern of the Cu–4Ni–4Sn alloy indicates a microstructure predominantly consisting of an FCC Cu (Ni, Sn) solid solution, together with a minor $Cu_{10}Sn_3$-type intermetallic phase, as evidenced by the appearance of additional minor diffraction peak at approximately 46.5°. The minor

peak observed here coincides with a characteristic diffraction peak of the ζ-$Cu_{10}Sn_3$ phase reported in the literature [22], and can be associated with a Ni-stabilized $Cu_{10}Sn_3$-type intermetallic phase. These findings align also with the thermodynamic predictions (Figs. 3 and 4), which indicate a broad stability range of the Cu-rich FCC solid solution for the investigated alloy compositions containing $\leq$ 3 wt% Sn. SEM micrograph and corresponding EDS map of the sintered Cu–4Ni alloy (Fig. 7) shows a porous microstructure with heterogenous distribution of elemental constituents, which can be primarily attributed to the limited diffusion of Ni across the Cu matrix during solid state sintering. The existence of considerable porosity within the microstructure correlates with the comparatively lower sintered density of the Cu–4Ni alloy.

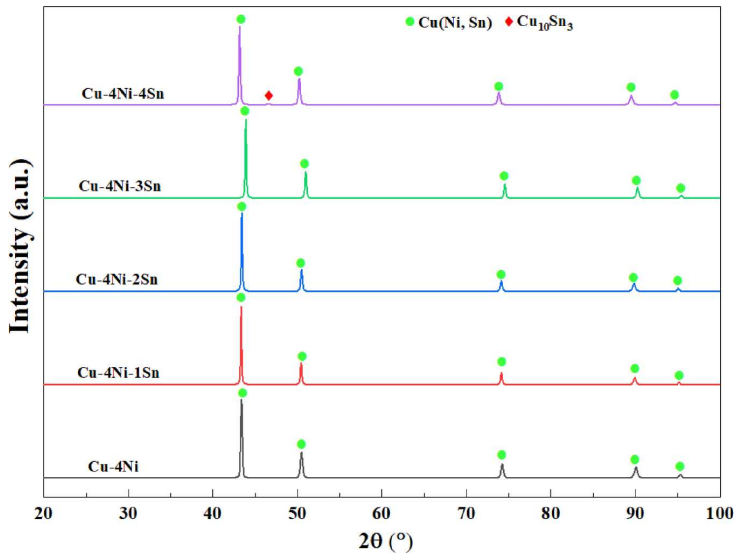


Figure 6: XRD patterns of the sintered Cu–Ni–Sn alloys.

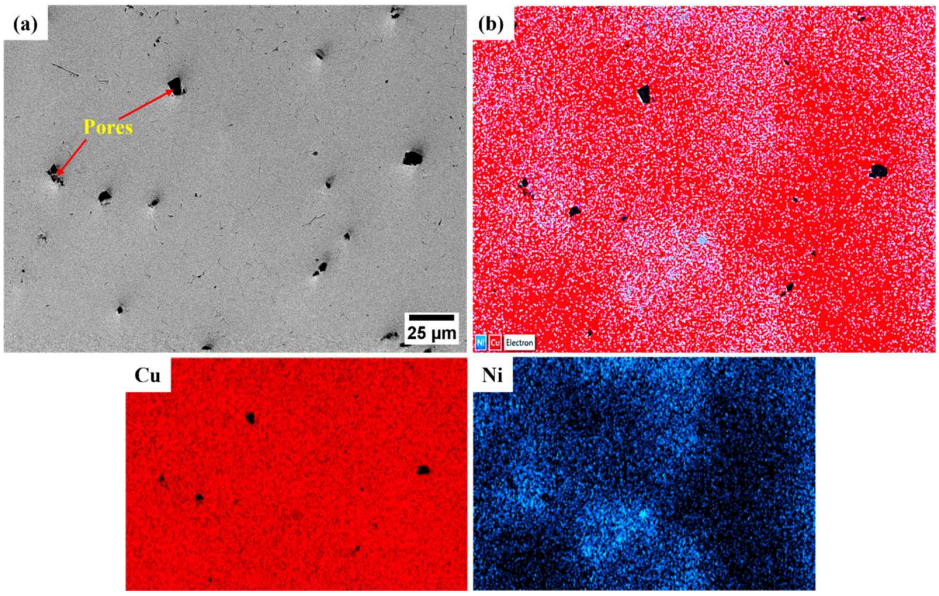


Figure 7: (a) BSE SEM image (magnification: 500 ×); and (b) EDS map of the sintered Cu–4Ni alloy.

The observed microstructure in the Cu–4Ni alloy can potentially be ascribed to the synergistic effects of diffusion asymmetry and vacancy evolution. The Cu–Ni system exhibits pronounced asymmetry in intrinsic diffusion behaviour, with substantially different diffusivities of Ni in Cu-rich regions and Cu in Ni-rich regions, which can contribute to a significant imbalance in atomic fluxes during interdiffusion [23]. This atomic flux imbalance can lead to generation of excess vacancies, resulting in a localized supersaturation of vacancies in areas where their formation surpasses annihilation at sinks such as particle surfaces, grain boundaries and other defects. In addition, the relatively weak vacancy-binding tendency of Ni [24], together with limited compensatory back-diffusion, may also hinder the effective annihilation of

these surplus vacancies. This implies that the surplus vacancies can progressively accumulate and cluster as the sintering process progresses, ultimately coalescing to form pores. With increase in temperature and passage of time, these pores tend to coalesce and coarsen so as to reduce the total surface free energy of the system, resulting in the porous microstructure observed in Cu–4Ni alloy.

On the contrary, the microstructural characteristics and elemental distribution in the Cu–4Ni–3Sn alloy (Fig. 8) specimen are markedly different from those in the Cu–4Ni alloy specimen. The SEM image and EDS mapping of the Cu–4Ni–3Sn alloy demonstrates a microstructure characterized by significant reduction in porosity and a more uniform distribution of solute elements throughout the Cu matrix. The decreased porosity observed in the Cu–4Ni–3Sn alloy is reflected in its higher sintered density, signifying a more effective densification process, which can be ascribed to the beneficial influence of Sn in pore elimination. Sn is known to exhibit a strong positive vacancy binding energy in Cu, promoting the formation of solute–vacancy complexes and altering vacancy distribution in a manner that facilitates vacancy-assisted pore shrinkage [24]. While vacancies are transported within the lattice, pore evolution is governed by the balance between vacancy creation and annihilation. In the absence of Sn, the surplus vacancies created owing to diffusion asymmetry may accumulate and coalesce leading to pore formation and subsequent pore growth. However, the inclusion of Sn is likely to affect this behaviour due to strong Sn-vacancy interactions that might reduce vacancy

clustering and facilitate vacancy annihilation at available sinks. In addition, the significantly higher intrinsic and interdiffusion coefficients of Sn relative to Ni are expected to facilitate diffusion-controlled mass transport, thereby promoting interparticle neck formation and pore reduction during sintering [25]. Consequently, the significantly improved densification and microstructural homogeneity observed in Cu–4Ni–3Sn alloy in comparison to the Cu–4Ni alloy can be attributed to the Sn induced enhancement of diffusion-controlled mass transport, coupled with expected promotion of vacancy annihilation resulting from the strong Sn-vacancy binding energy in Cu, thereby facilitating more effective pore elimination.

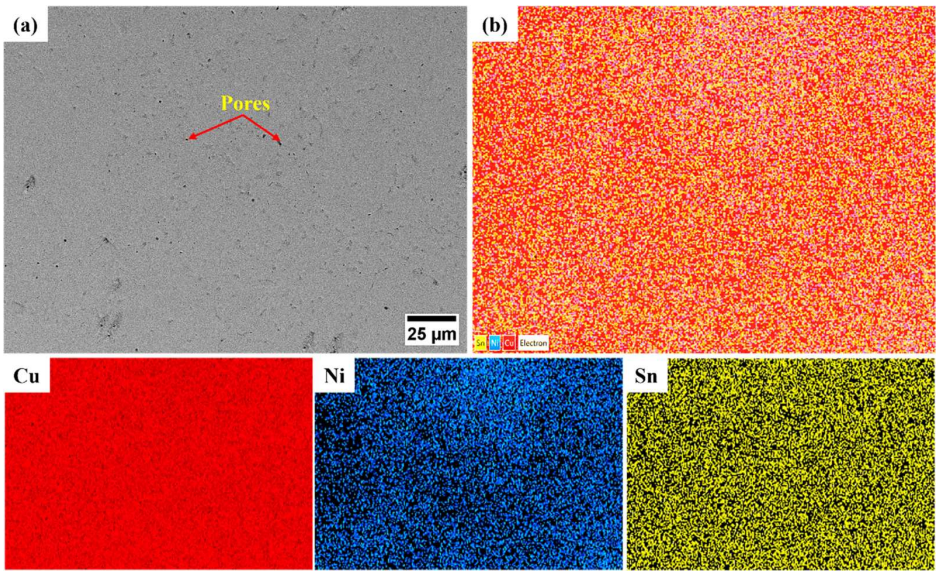


Figure 8: (a) BSE SEM image (magnification: 500 ×); and (b) EDS map of the sintered Cu–4Ni–3Sn alloy.

Meanwhile, the high-resolution BSE-SEM images displayed in Fig. 9 (acquired at magnifications ranging from 8000 × to 10,000 ×) reveal the existence of an intermetallic phase in both the Cu–4Ni–3Sn and Cu–4Ni–4Sn alloys. This intermetallic phase is present as discrete precipitates (bright white regions) embedded within the Cu-rich matrix (dark-grey regions). The precipitates are comparatively sparse and finer in the Cu–4Ni–3Sn alloy [Fig. 9(a, c)], whereas the Cu–4Ni–4Sn alloy exhibits a noticeably higher precipitate fraction and comparatively larger precipitates [Fig. 9(b, d)]. The increase in precipitate fraction with increasing Sn content from 3 to 4 wt% Sn aligns with the phase-fraction evolution predicted by CALPHAD (Fig. 4), which indicates a pronounced increase in secondary intermetallic phase formation when Sn content reaches 4 wt% Sn.

The relatively low precipitate fraction and finer size in Cu–4Ni–3Sn alloy result in a limited diffracting volume and consequently weak diffraction intensity, such that no discernible intermetallic phase peak is observed in the XRD pattern. In contrast, the greater precipitate fraction and coarser morphology in Cu–4Ni–4Sn alloy provide a larger effective diffracting volume, enabling a distinct intermetallic phase peak to be detected. Furthermore, the EDS line-scan profiles and point-compositional analysis, with the latter presented as bar graphs in Fig. 9(e–h), indicate that precipitates are enriched in Sn and Ni relative to the surrounding Cu-rich matrix. With increasing Sn content from 3 to 4 wt%, the Cu, Ni, and Sn concentrations exhibit higher standard deviations in both the matrix and precipitates, indicating

increased local compositional heterogeneity [Fig. 9(g, h)]. Notably, the intermetallic phase identified from the XRD pattern corresponds to a Ni-stabilized $Cu_{10}Sn_3$-type intermetallic, and the EDS point compositional analyses likewise reveal substantial Ni incorporation within the corresponding precipitate regions. The precipitates in Cu–4Ni–3Sn alloy exhibit an average composition of approximately 39 at% Cu, 34 at% Ni, and 27 at% Sn, whereas those in Cu–4Ni–4Sn comprise approximately 38 at% Cu, 36 at% Ni, and 26 at% Sn. The corresponding (Cu+Ni)/Sn atomic ratios of approximately 2.70 and 2.85, respectively, approach the 3:1 stoichiometric relationship characteristic of $(Cu,Ni)_3Sn$-type intermetallic phase. In this regard, the experimentally determined precipitate compositions exhibit closer compositional correspondence with the high-temperature γ-$(Cu,Ni)_3Sn$ phase predicted by the present Thermo-Calc calculations (Table 2) than with the idealized binary $Cu_{10}Sn_3$ composition. The apparent coexistence of a $Cu_{10}Sn_3$-type structural identity with a nearly 3:1 (Cu+Ni)/Sn stoichiometry is not inherently unusual; rather it indicates that the $Cu_{10}Sn_3$-type phase identified from the XRD pattern accommodates substantial substitution of Ni for Cu within the intermetallic framework. The noticeable presence of Ni within the corresponding precipitate regions is consistent with the reported ability of Ni to substitute for Cu and stabilize $Cu_{10}Sn_3$-type intermetallic phase in the Cu–Ni–Sn system [22]. Experimental phase-equilibrium studies have also

demonstrated significant substitution of Ni for Cu in Cu–Sn-based intermetallic phases, resulting in considerable compositional flexibility while retaining the underlying intermetallic structural framework [26, 27]. Such substitution is facilitated by their similar crystal structures and atomic size compatibility and their ability to occupy equivalent substitutional sites within the intermetallic framework. Taken together, the XRD phase identification, EDS compositional characteristics and CALPHAD predictions indicate that the experimentally observed secondary phase can be most appropriately described as a Ni-containing Cu–Sn intermetallic phase exhibiting $Cu_{10}Sn_3$-type diffraction characteristics and substantial Cu/Ni substitution, rather than being interpreted as an ideally stoichiometric $Cu_{10}Sn_3$ phase.

Moreover, the difference between the experimentally measured precipitate compositions and the corresponding equilibrium phase compositions predicted by Thermo-Calc (Table 2) arises from the fundamentally different nature of the two approaches. The CALPHAD calculations describe the equilibrium phase composition under the specified thermodynamic conditions in contrast to the non-equilibrium conditions prevailing during powder metallurgical processing. Furthermore, sintering involves finite diffusion distances and times which may limit complete elemental redistribution and homogenization and thereby produce microscale compositional variations within and among individual precipitates. Also, EDS measurements provide the local elemental composition of the specific precipitate regions sampled within the

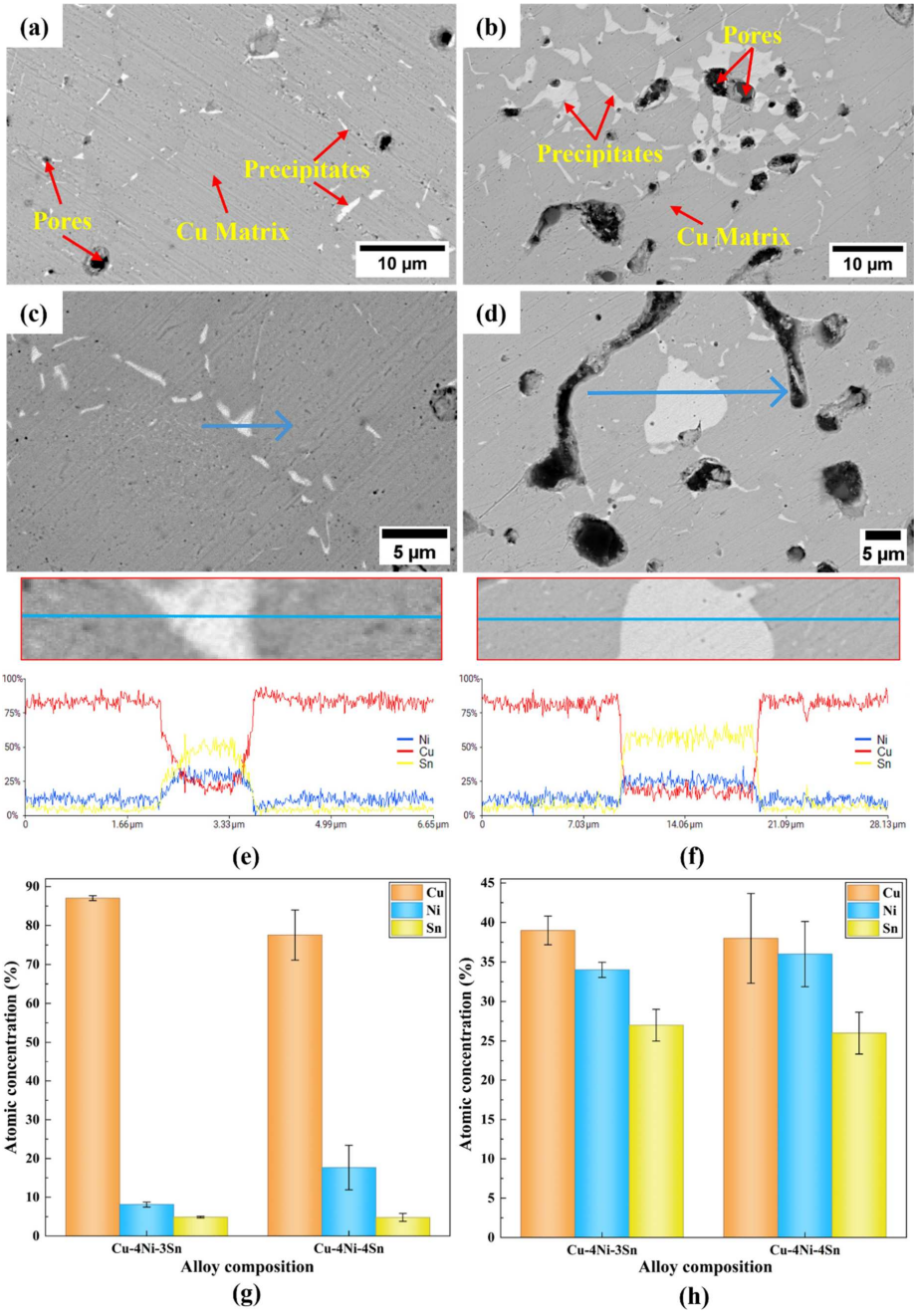


Figure 9: BSE SEM image illustrating the Cu-matrix and solute enriched precipitates in (a, c) Cu–4Ni–3Sn alloy and (b, d) Cu–4Ni–4Sn alloy and corresponding EDS line and point analysis results of (e, g) Cu–4Ni–3Sn alloy and (f, h) Cu–4Ni–4Sn alloy.

microstructure of the sintered alloy. Accordingly, the experimentally measured composition should be regarded as the local composition of the analysed precipitate region rather than as a unique stoichiometric composition of the phase. The present interpretation is confined to correlations supported by the phase constitution and local compositional data obtained in this study. A definitive and comprehensive characterization of the crystallographic structure and atomic scale chemical distribution of the Ni-containing intermetallic phase is beyond the scope of the present work, which focuses on elucidating the influence of compositional variation on the resulting properties of the sintered Cu–Ni–Sn alloys. Future studies employing transmission electron microscopy (TEM), complemented by selected-area electron diffraction and nanoscale chemical analysis, would be valuable for further elucidating the detailed crystal structure, compositional homogeneity, morphology, and possible compositional gradients of this intermetallic phase.

3.4. Hardness and electrical conductivity

Fig. 10 illustrates the effect of Sn content on the hardness and electrical conductivity of the sintered Cu–Ni–Sn alloys. The progressive increase in hardness with Sn addition is attributed to enhanced densification. This trend is consistent with the hardness–porosity relationship (Eq. (4)), which indicates that increasing relative density (R) leads to higher hardness due to reduced pore fraction [28].

$$\frac{H_R^2}{H_0^2} = \frac{R^2 - R_c^2}{1 - R_c^2} \tag{4}$$

where, H_0 and H_R represent the hardness of fully dense and partly dense material, respectively. R is the relative density and R_c is a constant having a value of $\sim$0.8 for metals.

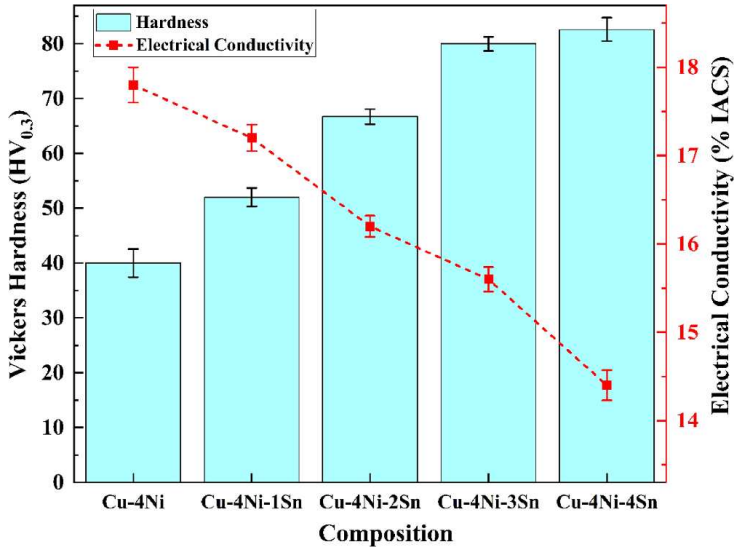


Figure 10: Variation of hardness and electrical conductivity with composition.

Simultaneously, Sn addition has also been reported to enhance hardness through solid-solution strengthening [13], which constitutes an important contribution to the overall increase in hardness. However, increase in hardness beyond 3 wt% Sn addition is marginal owing to reduced density in Cu–4Ni–4Sn alloy. In contrast, the electrical conductivity shows a decreasing trend with increasing Sn addition, with a significant reduction occurring

at 4 wt% Sn. The variation in electrical conductivity of the Cu–Ni–Sn alloys can be understood by correlating the resistivity with the densification and microstructural evolution. The resistivity of a multicomponent alloy is influenced by various factors including electrical resistance of porosity, vacancies, grain boundaries, solute atoms and precipitates [5]. The reduction in sintered density observed for the Cu–4Ni–4Sn alloy results in a higher porosity content and consequently increases pore-related electron scattering, thereby contributing to the reduction in electrical conductivity. In addition, the concentration of Ni and Sn retained in solid solution within the Cu-matrix contributes to electron scattering. The corresponding increase in resistivity due to solute scattering (ΔR_s) can be expressed as follows [29]:

$$\Delta R_s = a_{Ni} c_{Ni} + a_{Sn} c_{Sn} \tag{5}$$

where a_{Ni} and a_{Sn} are the respective resistivity concentration coefficients of Ni and Sn, and c_{Ni} and c_{Sn} denote their concentrations retained in solid solution within the Cu-rich matrix. The higher concentrations of Ni and Sn dissolved in the Cu-rich matrix of the Cu–4Ni–4Sn alloy [Fig. 9(g)] introduce greater local lattice distortion, which enhances electron scattering and thereby increases electrical resistivity, resulting in a corresponding reduction in electrical conductivity. The formation of secondary phases provides an additional contribution to the reduction in electrical conductivity by introducing regions of higher electrical resistivity within the Cu-rich matrix.

Within an effective-medium description, the increase in resistivity caused by precipitate scattering, ΔR_p can be represented using the Maxwell–Garnett relationship [30, 31]:

$$\Delta R_p = \frac{R_{\text{phase}} + 2R_0 + 2f\,(R_{\text{phase}} - R_0)}{R_{\text{phase}} + 2R_0 - 2f\,(R_{\text{phase}} - R_0)} \tag{6}$$

where R_{phase} is the resistivity of the secondary phase, R_0 is the resistivity of the Cu-rich matrix, and f is the volume fraction of the secondary phase. The thermodynamic calculations and microstructural observations presented in Fig. 4 and Fig. 9 indicate the formation of secondary phases, with their presence being more pronounced in the Cu–4Ni–4Sn alloy. Since these intermetallic phases possess substantially higher electrical resistivity than the Cu-rich matrix [30], their formation can significantly impede electron transport and consequently contribute to the reduction in electrical conductivity. Thus, the pronounced decrease in electrical conductivity at 4 wt% Sn addition in the Cu–Ni–Sn alloys can be attributed to the combined effects of increased secondary intermetallic phase formation, greater residual porosity and a higher concentration of Ni and Sn retained in the Cu-rich solid solution. These microstructural and compositional features collectively intensify electron scattering and thereby reduce the electrical conductivity of the alloy.

3.5. Compression response

The compressive stress–strain curves of the sintered Cu–Ni–Sn alloys presented in Fig. 11(a) exhibit a progressive increase in flow stress with increasing strain beyond yielding, indicative of sustained plastic deformation accompanied by pronounced work hardening. A distinct difference is observed in the nature of the elastic–plastic transition between the investigated compositions. The Cu–4Ni compact exhibits a relatively diffuse transition from elastic to plastic deformation, whereas the Cu–4Ni–3Sn alloy displays a more clearly defined yield point together with a higher compressive yield strength. The observed contrasting elastic–plastic transition in the sintered compacts may be interpreted in terms of the deformation behaviour of the sintered porous compacts. Green's plasticity theory for porous solids establishes that the yielding of a porous material is governed by both the deviatoric and hydrostatic components of the internal stress, with the yield surface contracting as the pore volume fraction increases [32]. Thus, in a porous sintered structure, the pores modify the local stress state, causing different microscopic regions to attain their local yield conditions at different levels of macroscopic stress owing to the spatial heterogeneity in pore size, morphology, and distribution.

At the microscale, local plastic "pockets" can initially form in the vicinity of pores, where they partially blunt the local stress concentrations and remain confined within the surrounding elastic field [33]. With continued deformation, these plastic regions progressively expand and interact until

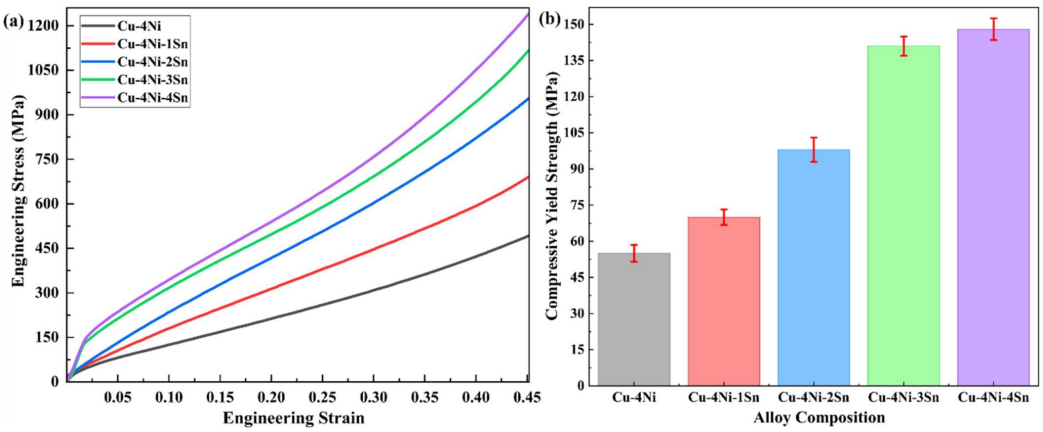


Figure 11: (a) Stress–strain curves under compressive loading; and (b) yield strength comparison of the sintered Cu–Ni–Sn alloys.

plasticity becomes sufficiently widespread for macroscopic yielding to be established. Consequently, yielding in a porous compact occurs progressively over a finite stress interval rather than initiating simultaneously across all regions of the material. This mechanism is particularly relevant to the relatively more porous Cu–4Ni compact, where the greater residual porosity and its spatial heterogeneity, together with the comparatively lower degree of sintering as reflected by its negative value of densification parameter [Fig. 5(b)], are associated with less-developed interparticle necks and a less continuous metallic load-bearing network. This microstructural condition can facilitate the distributed activation of local plastic deformation over a broader range of macroscopic stress, thereby contributing to the observed diffuse elastic–plastic transition. In contrast, the substantially higher densification and lower residual porosity of the Cu–4Ni–3Sn compact indicate a more continuous and effectively consolidated metallic skeleton. The higher degree of

densification is indicative of more extensive interparticle bonding and associated neck development during sintering, which reduces the extent of interconnected pore space and promotes a more continuous load-bearing network. Consequently, the development of pore-mediated local plasticity is expected to be less extensive, allowing widespread plastic flow to be established over a comparatively narrower stress interval and giving rise to the more clearly defined yield transition observed for Cu–4Ni–3Sn alloy. Moreover, the more than two-fold increase in compressive yield strength of the Cu–4Ni–3Sn alloy relative to the Cu–4Ni alloy, as shown in Fig. 11(b), can, from a comparative perspective, be primarily associated with the higher relative sintered density of the former and the strengthening effects associated with the incorporation of Sn. Increased densification has been reported to enhance the effective load-bearing fraction of sintered compacts while mitigating pore-induced stress concentrations and strain localization, thereby increasing their resistance to plastic deformation [34, 35]. Accordingly, the role of densification in the present study is considered primarily in relation to its contribution to the difference in macroscopic yield strength between the two alloys. In contrast, the strengthening effects associated with Sn incorporation are specific to the Cu–4Ni–3Sn alloy and can be subsequently resolved into their individual contributions. Consequently, the subsequent section delves into the sintering characteristics that contribute to the improved densification observed in the Cu–4Ni–3Sn alloy, as well as the strengthening mechanisms that govern its yield strength.

4. Discussion

4.1. Sintering characteristics

To identify the mechanism responsible for the improved densification response of the Cu–4Ni–3Sn alloy relative to the Cu–4Ni alloy, thermal response of the sintered compacts during heating was studied by employing differential scanning calorimetry (DSC). Fig. 12 illustrates a distinct difference in the thermal behaviour of the Cu–4Ni and Cu–4Ni–3Sn alloys, indicating that the sintering mechanism differs substantially in the investigated alloys. The Cu–4Ni alloy exhibited a continuous increase in heat flow without any noticeable thermal phenomenon, implying that no melting or phase transformation occurs during the initial heating phase. Thus Cu–4Ni alloy sinters entirely through solid-state sintering, where neck growth and pore elimination are governed by diffusion-controlled mass transport. On the other hand, Sn can give rise to liquid phase formation during the initial heating stage owing to its low melting point (∼232 °C). This is evident from the DSC curve of Cu–4Ni–3Sn alloy [Fig. 12(b)], which reveals a distinct endothermic peak at approximately 232 °C, corresponding to the melting of Sn containing regions during heating.

This observation provides experimental evidence for the formation of a transient liquid phase which dissolves into the Cu matrix prior to reaching the sintering temperature. Therefore, the enhanced densification of the Cu–4Ni–3Sn alloy can be attributed to a two-stage mechanism comprising an initial transient liquid-assisted particle rearrangement during heating, followed by

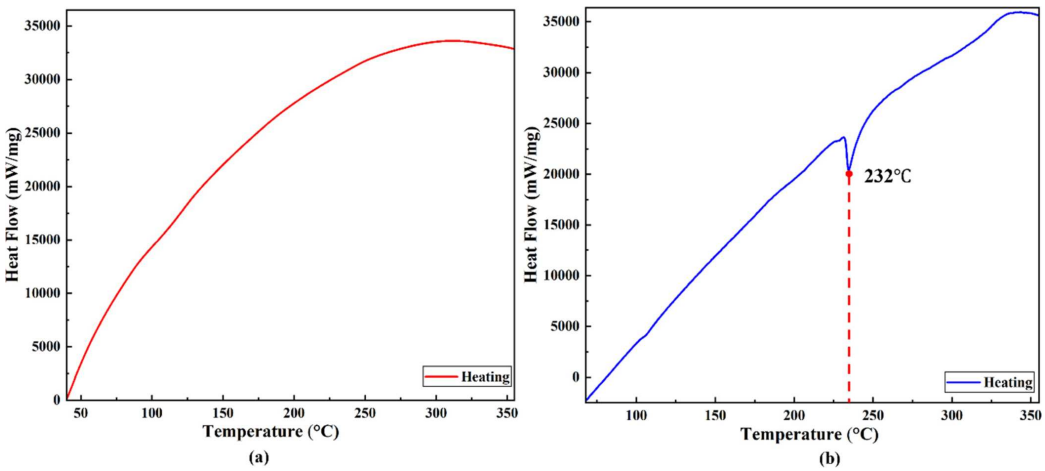


Figure 12: DSC curves of (a) Cu–4Ni and (b) Cu–4Ni–3Sn alloys.

diffusion-controlled solid-state sintering at 900 °C. The transient liquid generated at particle contacts is expected to facilitate capillary-driven particle rearrangement and improve interparticle wetting, thereby expediting mass transport through rapid diffusion and accelerated neck formation. These beneficial effects provide a plausible basis for the effective pore elimination during sintering, resulting in higher densification of the Cu–4Ni–3Sn alloy as compared to the Cu–4Ni alloy. The occurrence of transient liquid-phase-assisted sintering could potentially be further linked to the solute distribution in the as-sintered microstructure. Subsequent to the preliminary liquid-phase formation associated with Sn melting, the resulting liquid progressively interacts with the Cu rich regions, and undergoes dissolution and diffusion into the matrix as heating continues. With continued thermal exposure, Sn is expected to progressively redistribute within the Cu-rich matrix, with its distribution governed by the temperature-dependent solubility of Sn in the

solid solution and the local chemical composition. Where localized Sn enrichment results in concentrations exceeding the equilibrium solubility of Sn in Cu, the supersaturated regions may facilitate the nucleation and growth of Sn-containing intermetallic phases.

The high-magnification BSE SEM image and the corresponding EDS maps presented in Fig. 13 provide additional microstructural evidence of the ensuing Sn redistribution, revealing the localized compositional variations developed during the subsequent stages of sintering. In particular, the matrix exhibits a predominantly uniform distribution of Cu, while localized Sn enrichment can be observed in regions adjacent to or surrounding the pores. This localized enrichment of Sn observed in the vicinity of the pores is consistent with the transient liquid phase sintering behaviour of the Cu–Sn system reported in the literature [36, 37]. Since the transient liquid exists only during the initial stage of the thermal cycle and subsequently undergoes dissolution, diffusion, and phase evolution, it is not expected to be retained as a distinct feature in the final as-sintered microstructure. Therefore, the DSC evidence of Sn melting, together with the high-magnification BSE SEM image and corresponding elemental distribution mapping, provides converging experimental evidence in support of the proposed transient liquid-phase assisted sintering mechanism.

In addition, an increased fraction of liquid phase at early stages may lead to pore isolation and possible gas entrapment, thereby adversely affecting

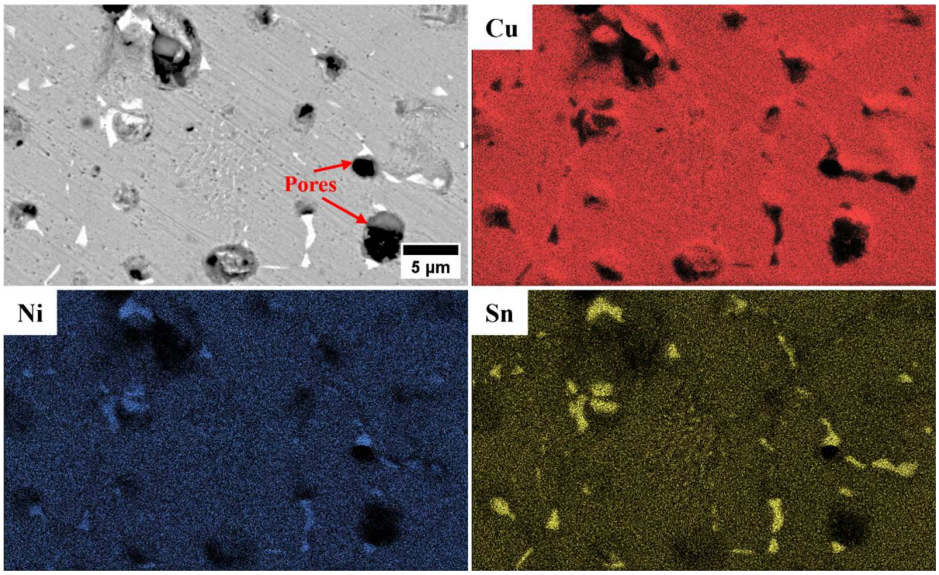


Figure 13: High magnification (12,000 ×) BSE-SEM image and corresponding elemental distribution map of Cu–4Ni–3Sn alloy.

the densification. As a result, with increased Sn addition (4 wt %), the densification behaviour is adversely affected, as evidenced by the reduction in sintered density [Fig. 5(a)] and the corresponding increase in porosity, accompanied by the formation of comparatively large and interconnected pores [Fig. 9(b, d)]. Such behaviour aligns with classical liquid-phase sintering theory as reported in previous works [38, 39] wherein excessive liquid formation can hinder pore elimination and lead to density stagnation or even degradation. The observed densification enhancement up to 3 wt% Sn addition is therefore attributed to the formation of an optimum liquid fraction that maximizes the beneficial effects of transient liquid-phase assisted sintering without introducing the adverse consequences associated with excessive liquid formation.

4.2. Strengthening mechanisms

4.2.1. Grain boundary strengthening

Grain boundaries serve as effective barriers to dislocation motion by obstructing the free glide of dislocations across adjacent grains. This obstruction impedes dislocation motion and hence increases the resistance of material to plastic deformation and thus contributes significantly to the strength enhancement. The density of grain boundaries, which is intrinsically governed by the grain size, further dictates the extent of this strengthening effect which can be quantitatively described by the Hall–Petch equation [40] represented as follows:

$$\sigma_{gbs} = \frac{k_h}{\sqrt{d}} \tag{7}$$

where k_h is a constant. d is the average grain size of the sintered Cu–4Ni–3Sn alloy. The IPF maps and grain size distribution plots shown in Fig. 14 illustrate the pronounced influence of Sn addition on the grain structure. Specifically, the average grain size reduced from approximately 18.05 μm in the Cu–4Ni alloy to approximately 9.66 μm in the Cu–4Ni–3Sn alloy, signifying a noteworthy grain refinement effect. According to Eq. (7), the grain boundary strengthening contribution in the Cu–4Ni–3Sn alloy is approximately 48.26 MPa.

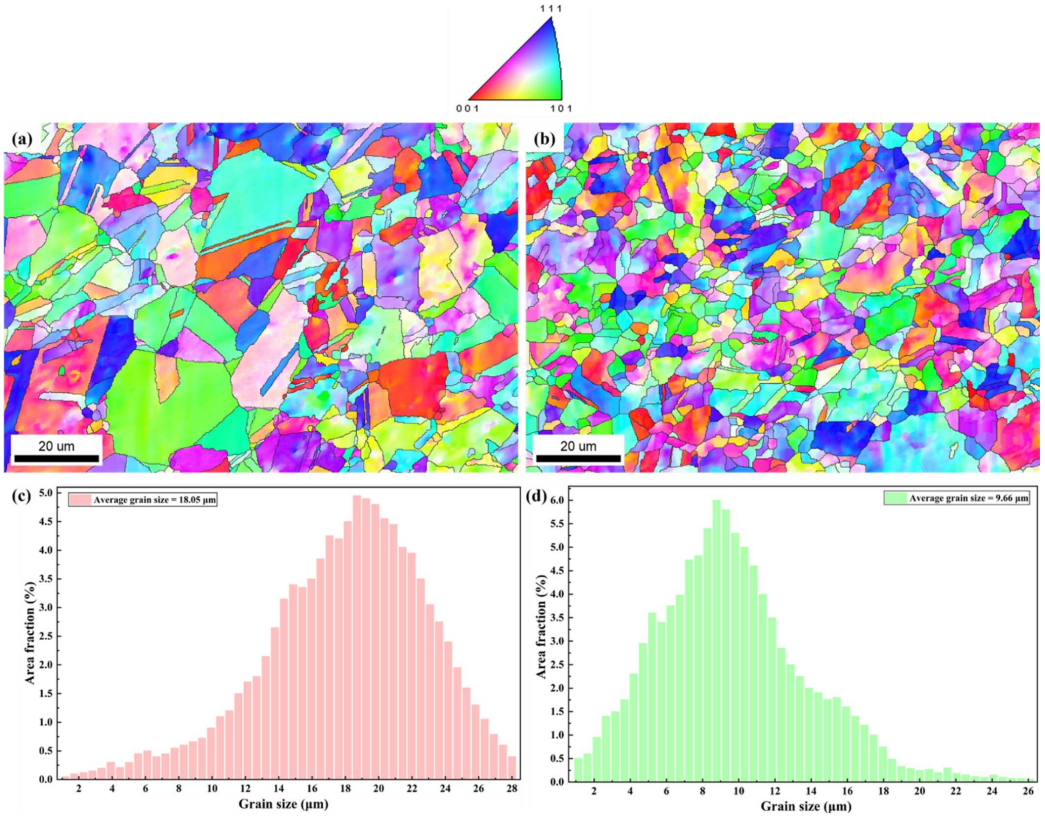


Figure 14: (a, b) Representative inverse pole figure (IPF) maps and (c, d) corresponding grain-size distributions of the Cu–4Ni and Cu–4Ni–3Sn alloys, respectively.

4.2.2. Precipitation strengthening

Since the size of the formed precipitates lies in the micrometer range, the Orowan strengthening mechanism, also referred to as dislocation bypassing, is considered the predominant strengthening mode. This mechanism can be described using the following equations [41, 42]:

$$\sigma_{orowan} = \frac{0.4MGb}{\pi\sqrt{1-\nu}} \frac{\ln\left(\frac{2\bar{r}_m}{b}\right)}{\lambda_p} \tag{8}$$

$$\bar{r}_m = \sqrt{\frac{2}{3}} r \tag{9}$$

$$\lambda_p = 2\bar{r}_m \left(\sqrt{\frac{\pi}{4f}} - 1 \right) \tag{10}$$

In this formulation, M, G, ν and b denote the Taylor factor, shear modulus, Poisson's ratio and Burgers vector respectively, while $\bar{r}_m$ represents mean radius of a circular cross-section in a random plane for a spherical precipitate and r denotes the average precipitate radius. The term λ_p corresponds to the inter-precipitate spacing, and f represents the volume fraction of precipitates present in the microstructure. By carrying out image analysis of the high-magnification BSE-SEM images of the Cu–4Ni–3Sn alloy, the average equivalent circular diameter of the precipitates was found to be approximately 0.6 μm, and the corresponding area fraction, which by the principle of Delesse [43] serves as an unbiased stereological estimator of the volume fraction for randomly distributed second-phase particles, was determined to be $\sim$0.02 (2%). Thus, the total precipitation strengthening contribution (calculated using Eqs. (8)–(10)) was estimated to be $\approx$ 16.17 MPa.

4.2.3. Dislocation strengthening

The Bailey–Hirsch formula (Eq. (11)) is typically used to determine the contribution of dislocation strengthening to the alloy strength [44, 45].

$$\sigma_d = \alpha G b \sqrt{\rho} \tag{11}$$

In this expression, α denotes a constant, with a value of 0.3 for copper. ρ represents the dislocation density, which can be estimated using the subsequent equation [46].

$$\rho = 16.1\frac{\varepsilon^2}{b^2} \tag{12}$$

where ε represents micro strain, which can be calculated from the XRD pattern of the sample by using the following relationship [47].

$$\beta\cos\theta = \frac{k\lambda}{d} + 4\varepsilon\sin\theta \tag{13}$$

Here, β denotes the full width at half maximum (FWHM) of the diffraction peak, λ represents the wavelength of Cu Kα radiation (0.154 nm), k is the Scherrer constant with an approximate value of 0.9, θ corresponds to the Bragg diffraction angle, and d indicates the crystallite size. Based on Eqs. (11)–(13), the dislocation strengthening contribution to the strength of the Cu–4Ni–3Sn alloy was estimated to be 25.28 MPa. The parameters utilised to calculate different strengthening contributions are listed in Table 3.

Table 3: Parameters employed for strengthening mechanisms calculations.

Parameter	Description	Units	Value	Reference
b	Burgers vector of Cu	nm	0.256	[48]
G	Shear modulus of Cu	GPa	45.5	[49]
M	Taylor factor	–	3.06	[7]
α	Geometric constant	–	0.3	[7]
ν	Poisson's ratio	–	0.324	[50]
k_h	Hall-Petch constant	MPa $\mathrm{m}^{1/2}$	0.15	[51]

4.2.4. Solid solution strengthening

The yield strength increment caused by solid solution strengthening can be expressed as per Eq. (14) [52].

$$\sigma_{ss} = \left(\sum_i k_i^{1/n} c_i \right)^n \tag{14}$$

where n is a constant taken to be $1/2$; c_i denotes the concentration of solute i, and k_i represents the strengthening constant for solute i. Because the solid-solution strengthening coefficient (k_i) has not been conclusively established for the solute lean Cu–Ni–Sn alloys in the available literature, direct calculation of the solid-solution strengthening contribution using empirical models is subject to considerable uncertainty. As a result, an indirect approach was adopted which was rooted in the additive nature of strengthening mechanisms, where the experimentally determined yield strength can be represented in the following form as the cumulative contribution of various strengthening mechanisms:

$$\sigma_y = \sigma_0 + \sigma_{gbs} + \sigma_{ss} + \sigma_{orowan} + \sigma_d \tag{15}$$

where, σ_y is the compressive yield strength, whose experimental value was determined to be $\approx$ 141 MPa [Fig. 11(b)], while σ_0 represents the friction stress of copper alloy. In the present analysis, σ_0 was taken as 20 MPa, based on the value reported in the literature [53]. The term σ_{gbs} denotes the contribution in yield strength arising from grain boundary strengthening, while σ_{ss},

σ_{orowan} and σ_d correspond to the strength contribution resulting from solid-solution strengthening, precipitation strengthening and dislocation strengthening, respectively. The contribution of solid-solution strengthening was determined by calculating the remainder after deducting the contributions of all other strengthening mechanisms from the experimental yield strength. Thus, the total solid-solution strengthening contribution was estimated to be 31.29 MPa. The solid-solution strengthening response of Cu–Ni–Sn alloys is governed by the interaction between solute atoms and the Cu lattice, which depends primarily on the difference in the atomic radius and the shear modulus between the solute atoms and Cu matrix [54]. The significant disparity in atomic radii between Sn and Cu can lead to a greater lattice distortion, which would amplify the lattice friction of interstitial atoms [55], resulting in impeding dislocation movement and strengthening the alloy. On the other hand, the contribution of Ni to solid-solution strengthening is expected to be relatively limited, since the atomic radius of Ni is close to that of Cu [13].

The estimated solid-solution strengthening contribution to yield strength should be interpreted as the cumulative effect of the alloying elements rather than an individual contribution from Ni and Sn, with the contribution from Sn expected to be more pronounced. Moreover, it is evident from the percentage contribution (Fig. 15), the dominant strengthening contributions in the Cu–4Ni–3Sn alloy arise from grain boundary strengthening and solid solution strengthening. The synergistic influence of these two mechanisms plays a crucial role in strength enhancement of the sintered alloy.

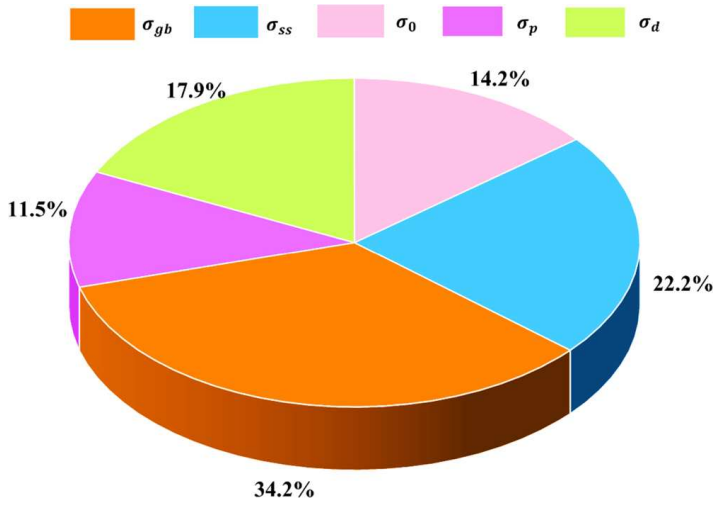


Figure 15: Percentage contribution of various strengthening mechanisms towards overall strengthening.

5. Conclusions

The principal conclusions of this study are summarized as follows:

1. CALPHAD calculations successfully delineated the phase-stability window, predicting that compositions up to 3 wt% Sn content are predominantly composed of Cu-rich FCC phase, with only a limited fraction of secondary intermetallic phase.
2. The thermodynamic predictions are in close agreement with the experimental findings which indicated that addition of 3 wt% Sn results in the formation of a microstructure dominated by the Cu-rich FCC matrix, accompanied by a limited amount of solute-enriched intermetallic phase in the sintered alloy.
3. Meanwhile, an increase in the concentration of Sn up to 3 wt%, resulted

in a remarkable increase in sintered density, hardness and compressive yield strength as compared to the Cu–4Ni alloy, which was mainly attributed to reduction in porosity, grain refinement and solid-solution strengthening.

4. Increasing the Sn concentration to 4 wt% induced a thermodynamic transition towards dual-phase stability, which was experimentally accompanied by inhibited densification and a marked deterioration in electrical conductivity, which was attributed to enhanced compositional partitioning and intermetallic phase formation.
5. Overall, this work establishes a composition–microstructure–property correlation identifying Cu–4Ni–3Sn alloy as a promising solute-lean composition for achieving a favourable combination of densification, strength and electrical conductivity.

CRediT authorship contribution statement

Tafzeelul Kamal: Writing – original draft, Visualization, Validation, Methodology, Investigation, Formal analysis, Data curation, Conceptualization. **Harish Ranot:** Writing – review & editing, Formal analysis. **Swapnadeep Mandal:** Writing – review & editing, Investigation. **Mirtunjay Kumar:** Writing – review & editing, Software. **Anish Upadhyaya:** Writing – review & editing, Resources.

Declaration of Competing Interest

The authors declare that they have no known competing financial interests or personal relationships that could have appeared to influence the work reported in this paper.

Data availability

Data will be made available on request.

References

[1] L. Guo, P. Zuo, Z. Zhang, Q. Zhang, M. Zhao, X. Hou, J. Wu, B. Zhang, A review of Cu–Ni–Sn alloys: processing, microstructure, properties, and developing trends, Materials 16 (2023) 444. doi:10.3390/ma16010444.

[2] H. Jiang, Z. Yang, L. Peng, H. Guo, H. Xie, D. Liu, Y. Cao, The thermal instability mechanism and annealed behavior of ultra-high strength Cu–Ni–Sn alloy, J. Alloys Compd. 1013 (2025) 178508. doi:10.1016/j.jallcom.2025.178508.

[3] B. Sankar, C. Vinay, J. Vishnu, K. V. Shankar, G. P. G. Krishna, V. Govind, A. J. Jayakrishna, Focused review on Cu–Ni–Sn spinodal alloys: from casting to additive manufacturing, Met. Mater. Int. 29 (2022) 1203–1228. doi:10.1007/s12540-022-01305-6.

[4] H. Jiang, L. Peng, X. Mi, H. Guo, H. Xie, D. Liu, F. Liu, Z. Yang, Simultaneously enhancing the strength and electrical conductivity of Cu–Ni–Sn alloy through plastic deformation of an intermetallic compound, Mater. Des. 235 (2023) 112445. doi:10.1016/j.matdes.2023.112445.

[5] Y. Zhang, X. Gan, Z. Xiao, Y. Jia, W. Qiu, X. Meng, Y. Zhang, L. Xiao, G. Sun, T. Zhang, Evolution of microstructure and properties of an ultrahigh strength Cu–Ni–Sn alloy with low Sn content during the multi-stage thermomechanical treatment, Mater. Sci. Eng. A 872 (2023) 144933. doi:10.1016/j.msea.2023.144933.

[6] J. C. Zhao, M. R. Notis, Spinodal decomposition, ordering transformation, and discontinuous precipitation in a Cu–15Ni–8Sn alloy, Acta Mater. 46 (1998) 4203–4218. doi:10.1016/S1359-6454(98)00095-0.

[7] B. Luo, D. Li, C. Zhao, Z. Wang, Z. Luo, W. Zhang, A low Sn content Cu–Ni–Sn alloy with high strength and good ductility, Mater. Sci. Eng. A 746 (2019) 154–161. doi:10.1016/j.msea.2018.12.120.

[8] M. Gao, Z. Chen, H. Kang, R. Li, W. Wang, C. Zou, T. Wang, Effects of Nb addition on the microstructures and mechanical properties of a precipitation hardening Cu–9Ni–6Sn alloy, Mater. Sci. Eng. A 715 (2018) 340–347. doi:10.1016/j.msea.2018.01.022.

[9] Z. Guo, J. Jie, S. Liu, Y. Zhang, B. Qin, T. Wang, T. Li, Effect of V addition on microstructures and mechanical properties of Cu–15Ni–8Sn

alloy, Mater. Sci. Eng. A 748 (2019) 85–94. doi:10.1016/j.msea.2019.01.084.

[10] Z. Guo, J. Jie, J. Liu, S. Yue, S. Liu, T. Li, Effect of cold rolling on aging precipitation behavior and mechanical properties of Cu–15Ni–8Sn alloy, J. Alloys Compd. 848 (2020) 156275. doi:10.1016/j.jallcom.2020.156275.

[11] S. S. Kim, J. C. Rhu, Y. C. Jung, S. Z. Han, C. J. Kim, Aging characteristics of thermomechanically processed Cu–9Ni–6Sn alloy, Scr. Mater. 40 (1998) 1–6. doi:10.1016/S1359-6462(98)00400-X.

[12] C. Guo, Y. Shi, J. Chen, X. Xiao, B. Liu, J. Liu, B. Yang, Effects of P addition on spinodal decomposition and discontinuous precipitation in Cu–15Ni–8Sn alloy, Mater. Charact. 171 (2021) 110760. doi:10.1016/j.matchar.2020.110760.

[13] M. Chen, X. Liu, F. Zhao, X. Xiao, W. Li, J. Xie, Elucidating the intrinsic composition-microstructure-property relationships of Cu–Ni–Sn alloys by integrating rapid fabrication, thermodynamic calculations, and machine learning, Mater. Sci. Eng. A 949 (2026) 149396. doi:10.1016/j.msea.2025.149396.

[14] F. Tan, W. Chen, Z. Zhao, Y. Jiang, J. Yu, Y. Li, H. Wu, J. He, G. Xu, M. Wang, Z. Li, Multiscale precipitation structures enabling ultrahigh

strength and high conductivity of Cu–Ni–Sn–In alloy, Mater. Sci. Eng. A 972 (2026) 150607. doi:10.1016/j.msea.2026.150607.

[15] J. Miettinen, Thermodynamic description of the Cu–Ni–Sn system at the Cu–Ni side, Calphad 27 (2003) 309–318. doi:10.1016/j.calphad.2003.10.001.

[16] W. Zhao, Y. Yang, E. Zhang, B. Zhang, M. Wen, Y. Tang, L. Zhang, Thermodynamic descriptions of the binary Ni–Sn and ternary Cu–Ni–Sn systems over entire composition range: a revisit, Calphad 75 (2021) 102344. doi:10.1016/j.calphad.2021.102344.

[17] J. O. Andersson, T. Helander, L. Höglund, P. Shi, B. Sundman, Thermo-Calc & DICTRA, computational tools for materials science, Calphad 26 (2002) 273–312. doi:10.1016/S0364-5916(02)00037-8.

[18] F. Li, W. Liu, C. Ding, S. Wang, X. Meng, The microstructures and properties of Cu–Ni–Co–Si alloys: a critical review, Metals 15 (2025) 564. doi:10.3390/met15050564.

[19] P. Kratochvíl, J. Mencl, J. Pešička, S. N. Komnik, The structure and low temperature strength of the age hardened Cu–Ni–Sn alloys, Acta Metall. 32 (1984) 1493–1497. doi:10.1016/0001-6160(84)90095-6.

[20] R. M. German, S. J. Park, Mathematical Relations in Particulate Materials Processing: Ceramics, Powder Metals, Cermets, Carbides,

Hard Materials, and Minerals, John Wiley & Sons, Hoboken, 2008. doi:10.1002/9780470370087.

[21] A. Upadhyaya, G. Sethi, Effect of heating mode on the densification and microstructural homogenization response of premixed bronze, Scr. Mater. 56 (2007) 469–472. doi:10.1016/j.scriptamat.2006.11.031.

[22] C. Wieser, W. Hügel, S. Martin, J. Freudenberger, A. Leineweber, Stabilization of the ζ-Cu10Sn3 phase by Ni at soldering-relevant temperatures, J. Electron. Mater. 49 (2020) 3609–3623. doi:10.1007/s11664-020-08036-7.

[23] B. Wierzba, W. Skibiński, The interdiffusion in copper-nickel alloys, J. Alloys Compd. 687 (2016) 104–108. doi:10.1016/j.jallcom.2016.06.085.

[24] T. Gorecki, C. Gorecki, K. Ksiazek, S. Wacke, Effective vacancy formation energy and the solute-vacancy binding energy in binary Cu-based alloys, Visnyk Lviv Univ. Ser. Phys. 40 (2007) 238–244.

[25] Y. Liu, C. Chen, D. Liu, Y. Du, S. Liu, X. Tao, Y. Ouyang, Diffusivities and atomic mobilities for FCC Cu–Ni–Sn alloys, Calphad 59 (2017) 84–89. doi:10.1016/j.calphad.2017.08.005.

[26] C. H. Lin, S. W. Chen, C. H. Wang, Phase equilibria and solidification properties of Sn–Cu–Ni alloys, J. Electron. Mater. 31 (2002) 907–915. doi:10.1007/s11664-002-0182-8.

[27] C. Schmetterer, M. Rodriguez-Hortala, H. Flandorfer, Enthalpies of formation of (Cu,Ni)3Sn, (Cu,Ni)6Sn5-HT and (Ni,Cu)3Sn2-HT, J. Phase Equilib. Diffus. 35 (2014) 429–433. doi:10.1007/s11669-014-0305-y.

[28] Y. Kim, M. H. Hong, S. H. Lee, E. P. Kim, S. Lee, J. W. Noh, The effect of yttrium oxide on the sintering behaviour and hardness of tungsten, Met. Mater. Int. 12 (2006) 245–248. doi:10.1007/BF03027538.

[29] S. Nagarjuna, K. Balasubramanian, D. S. Sarma, Effect of Ti additions on the electrical resistivity of copper, Mater. Sci. Eng. A 225 (1997) 118–124. doi:10.1016/S0921-5093(96)10578-5.

[30] X. Pan, H. Zhu, B. Li, H. Zhuang, W. Qiu, Y. Yao, Z. Xia, S. Gong, Synergistic strengthening through Ni2MnSn nanocrystals and nano-precipitates achieves ultrahigh-strength in Cu–Ni–Mn–Sn alloy, Mater. Sci. Eng. A 961 (2026) 150201. doi:10.1016/j.msea.2026.150201.

[31] Y. Li, C. Liu, P. Li, T. Lu, C. Chen, Z. Guo, Y. Su, L. Qiao, J. Zhou, Y. Bai, Scattering cancellation by a monolayer cloak in oxide dispersion-strengthened alloys, Adv. Funct. Mater. 30 (2020) 2003270. doi:10.1002/adfm.202003270.

[32] R. J. Green, A plasticity theory for porous solids, Int. J. Mech. Sci. 14 (1972) 215–224. doi:10.1016/0020-7403(72)90063-X.

[33] T. I. Zohdi, M. Kachanov, I. Sevostianov, On perfectly plastic flow

in porous material, Int. J. Plast. 18 (2002) 1649–1659. doi:10.1016/S0749-6419(02)00005-0.

[34] Y. Huang, Z. Wang, L. Zhang, S. Wei, Pore/skeleton structure and compressive strength of porous Mo3Si-Mo5Si3-Mo5SiB2 intermetallic compounds prepared by spark plasma sintering and homogenization treatment, J. Alloys Compd. 856 (2021) 158150. doi:10.1016/j.jallcom.2020.158150.

[35] E. Zhang, B. Wang, On the compressive behaviour of sintered porous coppers with low to medium porosities—Part I: experimental study, Int. J. Mech. Sci. 47 (2005) 744–756. doi:10.1016/j.ijmecsci.2004.12.011.

[36] R. Tongsri, N. Tosangthum, T. Yotkaew, P. Muthitamongkol, A. Sri-On, U. Patakham, Characterization of liquid-phase sintered materials produced from mechanically alloyed Cu + Sn powder compacts, Mater. Charact. 113 (2016) 52–59. doi:10.1016/j.matchar.2016.01.001.

[37] X. Peng, Y. Wang, W. Wang, Z. Ye, J. Yang, J. Huang, Kinetics of Cu6Sn5 and Cu3Sn intermetallic compounds growth and isothermal solidification during Cu–Sn transient liquid phase sintering process, J. Alloys Compd. 949 (2023) 169631. doi:10.1016/j.jallcom.2023.169631.

[38] R. M. German, P. Suri, S. J. Park, Review: liquid phase sintering, J. Mater. Sci. 44 (2009) 1–39. doi:10.1007/s10853-008-3008-0.

[39] S. M. Lee, S. J. L. Kang, Theoretical analysis of liquid-phase sintering: pore filling theory, Acta Mater. 46 (1998) 3191–3202. doi:10.1016/S1359-6454(97)00489-8.

[40] N. Hansen, Hall–Petch relation and boundary strengthening, Scr. Mater. 51 (2004) 801–806. doi:10.1016/j.scriptamat.2004.06.002.

[41] G. Peng, X. Gan, Y. Jiang, Z. Li, K. Zhou, Hot isostatic pressing of Cu–15Ni–8Sn alloy with suppressed Sn macro-segregation and enhanced mechanical properties, Mater. Sci. Eng. A 855 (2022) 143866. doi:10.1016/j.msea.2022.143866.

[42] K. Ma, H. Wen, T. Hu, T. D. Topping, D. Isheim, D. N. Seidman, E. J. Lavernia, J. M. Schoenung, Mechanical behaviour and strengthening mechanisms in ultrafine grain precipitation-strengthened aluminium alloy, Acta Mater. 62 (2014) 141–155. doi:10.1016/j.actamat.2013.09.042.

[43] T. M. Mayhew, L.-M. C. Orive, Caveat on the use of the Delesse principle of areal analysis for estimating component volume densities, J. Microsc. 102 (1974) 195–207. doi:10.1111/j.1365-2818.1974.tb03979.x.

[44] J. E. Bailey, P. B. Hirsch, The dislocation distribution, flow stress, and

stored energy in cold-worked polycrystalline silver, Philos. Mag. 5 (1960) 485–497. doi:10.1080/14786436008238300.

[45] J. Kai-Xuan, Z. Yan-Jun, Y. Ran, S. Ke-Xing, L. Ya-Hui, Z. Yan-Min, Y. Shao-Dan, Z. Fei, H. Kuan, L. Dong-Dong, Y. Wen-Hao, Effects of cold deformation and aging on the phase transformation and mechanical properties of a Cu–15Ni–8Sn alloy, Mater. Charact. 210 (2024) 113796. doi:10.1016/j.matchar.2024.113796.

[46] G. K. Williamson, R. E. Smallman, Dislocation densities in some annealed and cold-worked metals from measurements on the X-ray Debye-Scherrer spectrum, Philos. Mag. 1 (1956) 34–46. doi:10.1080/14786435608238074.

[47] G. K. Williamson, W. H. Hall, X-ray line broadening from filed aluminium and wolfram, Acta Metall. 1 (1953) 22–31. doi:10.1016/0001-6160(53)90006-6.

[48] J. Gubicza, N. Q. Chinh, G. Krállics, I. Schiller, T. Ungár, Microstructure of ultrafine-grained FCC metals produced by severe plastic deformation, Curr. Appl. Phys. 6 (2006) 194–199. doi:10.1016/j.cap.2005.07.039.

[49] Q. Lei, Z. Li, A. Zhu, W. Qiu, S. Liang, The transformation behaviour of Cu–8.0Ni–1.8Si–0.6Sn–0.15Mg alloy during isothermal heat treatment,

Mater. Charact. 62 (2011) 904–911. doi:10.1016/j.matchar.2011.06.008.

[50] Y. Zhang, X. Gan, X. Wang, L. Li, X. Jiang, X. Meng, Z. Xiao, Microstructure and mechanical properties of a Cu–Ni–Sn–Si–Al alloy produced by equal channel angular pressing, Mater. Today Commun. 39 (2024) 108968. doi:10.1016/j.mtcomm.2024.108968.

[51] X. Chen, X. Xiao, D. Yuan, J. Chen, Y. Wu, Effect of Ni/Sn ratio on microstructure and properties of Cu–Ni–Sn–P alloy, Sci. Rep. 14 (2024) 31609. doi:10.1038/s41598-024-80079-w.

[52] H. A. Roth, C. L. Davis, R. C. Thomson, Modelling solid solution strengthening in nickel alloys, Metall. Mater. Trans. A 28 (1997) 1329–1335. doi:10.1007/s11661-997-0268-2.

[53] M. Gholami, J. Vesely, I. Altenberger, H. A. Kuhn, M. Janecek, M. Wollmann, L. Wagner, Effects of microstructure on mechanical properties of CuNiSi alloys, J. Alloys Compd. 696 (2017) 201–212. doi:10.1016/j.jallcom.2016.11.233.

[54] Y. Shi, C. Guo, J. Chen, X. Xiao, H. Huang, B. Yang, Recrystallization behaviour and mechanical properties of a Cu–15Ni–8Sn(P) alloy during prior deformation and aging treatment, Mater. Sci. Eng. A 826 (2021) 142025. doi:10.1016/j.msea.2021.142025.

[55] H. W. King, Quantitative size-factors for metallic solid solutions, J. Mater. Sci. 1 (1966) 79–90. doi:10.1007/BF00549722.